Solar Energy 262 (2023) 111909

Contents lists available at ScienceDirect

Solar Energy

journal homepage: www.elsevier.com/locate/solener

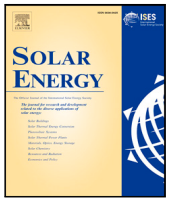

# Artificial neural network-based fault detection and isolation in a parabolic-trough solar plant with defocusing strategy

Sara Ruiz-Moreno *, Antonio J. Gallego, Eduardo F. Camacho

*Dept. de Ingeniería de Sistemas y Automática, University of Seville, Camino de los Descubrimientos, E-41092, Seville, Spain*

ARTICLE INFO

*Keywords:*
Fault detection
Fault diagnosis
Solar thermal power plant
Artificial neural network
Defocusing

ABSTRACT

Fault detection is crucial for ensuring optimal operation and maintenance of solar plants. This paper proposes a methodology for fault detection and isolation using artificial neural networks (ANNs) in a model of a 50 MW parabolic-trough solar plant that employs a defocusing strategy. The proposed methodology focuses on detecting three different types of faults in the collector area, namely, faults in the optical efficiency, flow rate, and thermal losses. The methodology is divided into three steps. Firstly, a feedforward dynamic neural network that internally models the concentrated parameter model of the system is used to detect faults and output the fault type. Secondly, information on the defocusing mechanism is added to the inputs of the neural network. Finally, the range of faults considered is adjusted based on the neural networks' ability to detect each fault size and its impact on the plant's outlet temperature. The accuracy of fault detection is evaluated through several simulations, and the proposed methodology shows promising results. The accuracy of fault detection is found to be 71.72%, 83.96%, and 90.62% for the first, second, and third approaches, respectively. The proposed methodology based on ANNs has the potential to improve the operational efficiency and reduce maintenance costs of solar plants.

## 1. Introduction

The use of renewable energies in industry is constantly increasing, either for electrical energy production applications or other purposes such as temperature regulation. This is mainly due to two factors: energy demand is always increasing and public awareness of the impact of non-renewable energies is growing. Accordingly, climate change and energy security have thus established themselves as the major concerns of the century [1]. In order to prevent climate change and global warming and to promote economic growth, it is necessary to promote the development of renewable and nuclear energy sources [2].

Solar energy is the oldest energy source [3] and is considered the cleanest renewable energy form [4]. In fact, solar thermal energy is a key element of the energy transition and serves as a good substitute for fossil fuels used for heat production [5]. This work is based on the use of parabolic trough collectors (PTCs), which are a type of solar thermal power plants.

A challenge for renewable energy sources, and more specifically solar energy, is that they are very dependent on weather conditions, which makes them difficult to predict and challenges the ability to control and maintain plant safety [6]. In addition, faults in solar collectors are highly coupled. For these reasons, the development of advanced fault detection techniques is of great importance.

Fault detection and diagnosis (FDD) [7] is a research field divided into two sections: fault detection, which aims to trigger some alarms after the appearance of a fault in a system, and fault diagnosis, which provides deeper information about the fault. The diagnosis part, in turn, is divided into two sections: fault isolation, which describes the fault type and location, and fault identification, which determines its magnitude. This work focuses on the subcategory of fault detection and isolation (FDI). FDD techniques can be divided into three types [8,9]: quantitative model-based methods based on mathematical relationships, qualitative model-based methods based on qualitative functions and process history-based methods that use historical data.

Until 1990s, most of the research in fault detection was developed in national defense, automobile industry, process plants, aircraft and nuclear power plants [7]. However, today it is becoming more and more widespread, with numerous recent applications in various fields and, specifically, in energy production. He et al. [10] apply multi-label learning for fault diagnosis in a photovoltaic array addressing the problem of faults coupling. Bououden et al. [11] propose an observer-based method for robust fault-tolerant control in wind turbine systems. Another fault-tolerant control approach is proposed by Zafra-Cabeza et al. [12] in the field of microgrids.

* Corresponding author.
*E-mail addresses:* srmoreno@us.es (S. Ruiz-Moreno), agallego2@us.es (A.J. Gallego), efcamacho@us.es (E.F. Camacho).

https://doi.org/10.1016/j.solener.2023.111909
Received 17 May 2023; Received in revised form 10 July 2023; Accepted 24 July 2023
Available online 3 August 2023

**Nomenclature**

| | |
|---|---|
| $\alpha$(t) | Fault multiplier – |
| $\delta_q$ | Flow rate additive fault |
| $\delta_s$ | Declination |
| $\omega_s$(t) | Hourly angle |
| $\phi$ | Latitude |
| $\rho(T)$ | Density kg/m$^3$ |
| $A$ | Pipe cross-sectional Area m$^2$ |
| $C(T)$ | Specific heat capacity J/(kg °C) |
| $eff_{def}$ | Defocus efficiency – |
| $G$ | Collector aperture m |
| $H_l(T)$ | Thermal loss coefficient W/(m$^2$ °C) |
| $H_t(T)$ | Convective heat transfer coefficient W/(m$^2$ °C) |
| $I(t)$ | Direct solar irradiance W/m$^2$ |
| $K_{opt}$ | Optical efficiency – |
| $L$ | Tube perimeter m |
| $L_{loop}$ | Loop length m |
| $n_o(t)$ | Geometric efficiency – |
| $n_{si}(\Delta t)$ | Number of defocusings in a period $\Delta t$ of the $i$th collector – |
| $q(t)$ | Volume flow rate m$^3$s |
| $S$ | Total area of the field m$^2$ |
| $s_{di}(t)$ | Defocusing state of the $i$th collector – |
| $t$ | Time s |
| $T(t)$ | Temperature °C |
| $x$ | Spacem |
| $X(t)$ | Neural network's input vector |
| $k$ | Timestep – |
| $f$ | Fluid |
| $in$ | Input |
| $loop$ | Mean for the entire loop |
| $m$ | Metal |
| $mean$ | Mean between input and output |
| $out$ | Output |
| ANN | Artificial neural network |
| DNI | Direct normal irradiance |
| FDD | Fault detection and diagnosis |
| FDI | Fault detection and isolation |
| HTF | Heat transfer fluid |
| PTC | Parabolic-trough collector |

Thermal solar plants are nonlinear systems with highly coupled faults, which hinders the problem of FDD with traditional methods. To solve this, a previous work [13] proposed a method based on a multi-label, multi-layer perceptron combined with a decoupling strategy. Machine learning techniques are great problem solvers that facilitate the detection of faults in complex systems and are on the rise, with recent applications in many different fields. Rodríguez et al. [14] apply recurrent neural networks to wind turbines for fault detection and offset error prediction. He et al. [10] propose the use of the k-nearest neighbor method with random forests and residual networks to classify different types of faults in photovoltaic systems. In the work by Ahmadipour et al. [15], a support vector machine is combined with the maximal overlap discrete wavelet packet transform and augmented Lagrangian particle swarm optimization to classify faults in a microgrid.

In the case of thermal solar systems, the number of existing applications in the literature is much lower because the faults in the collectors area are highly coupled, focusing mainly on just fault detection and in hot water systems. The work by Correa-Julian et al. [16] analyzes different deep learning techniques for fault detection and performance prediction, and Jiang et al. [17] propose the use of support vector machines to classify types of faults in solar water systems. Schmelzer et al. [18] propose a method based on fractional solar consumption for fault detection in a solar combi system. A more specific application is the work by Brennet et al. [19], which focuses on soiling determination in PTCs.

This work proposes an FDI approach for faults located in the collectors area and takes into account three types of faults: faults in the optical efficiency, flow rate and thermal loses. Moreover, it analyzes the effect of each type and size of fault on the plant output. In accordance with this analysis, this work proposes a range of fault sizes that are detectable by the neural networks (ANNs). This range is based on a combination of the neural network's ability and the fault effect.

Commercial solar plants are equipped with a defocusing mechanism to reduce the energy due to safety limitations. This makes the FDD problem even more complex since the reflectivity reduction due to the defocusing can be confused with an optical efficiency fault, as they affect the system similarly. This paper proposes the use of artificial neural networks that take into account some information of the defocusing strategy to improve the ability of distinguishing both effects. Previous works [20,21] focused on isolating faults with artificial neural networks in the ACUREX plant, a small, experimental plant without defocusing mechanism, which is an important mechanism included in all commercial plants.

The contributions of this paper compared with the previous works are the following:

- Fault detection and isolation in a model of a solar thermal plant of 50 MW that includes a defocusing strategy.
- Use of the defocusing angle and number of defocusings during a time horizon as inputs to the neural networks.
- Analysis of the faults effect on the outlet temperature.
- Selection of a new range of faults of each type.

The remainder of this paper is as follows. Section 2 gives a description of the system, the defocusing strategy and the faults considered. Section 3 provides an overview of the neural networks applied. Next, the methodology is described in Section 4 and a summary of the results is provided in Section 5 together with a discussion. The conclusions and future work are given in Section 6. In Appendix, two dynamic models are provided: one for simulation and the second one for designing purposes.

## 2. Description of the system

A parabolic trough collector plant is a type of solar thermal facility composed by several loops of parabolic mirrors, as shown in Fig. 1. Each of these mirrors receives solar direct normal irradiance (DNI) and reflects it onto its focal line. Along the focal line, there is placed a pipe that contains the heat transfer fluid (HTF) circulating. The fluid gets heated up by the DNI and then is directed to a heat exchanger, where it produces steam to drive a turbine generator.

This work uses a model of a 50 MW plant [22] that contains 90 loops of 620 m with 4 collectors each one. The collectors are north–south aligned and have a tracking system that makes them rotate around an axis that is parallel to the pipe to track the sun. The active part of the loop is the one that receives solar radiation and is 593 m long. The heat transfer fluid is Therminol VP-1 [23]. The nominal operating temperature is about 390–393 °C. The plant is simulated using the distributed parameter model, and the concentrated parameter model is used for control and FDD purposes. Both are described in Appendix.

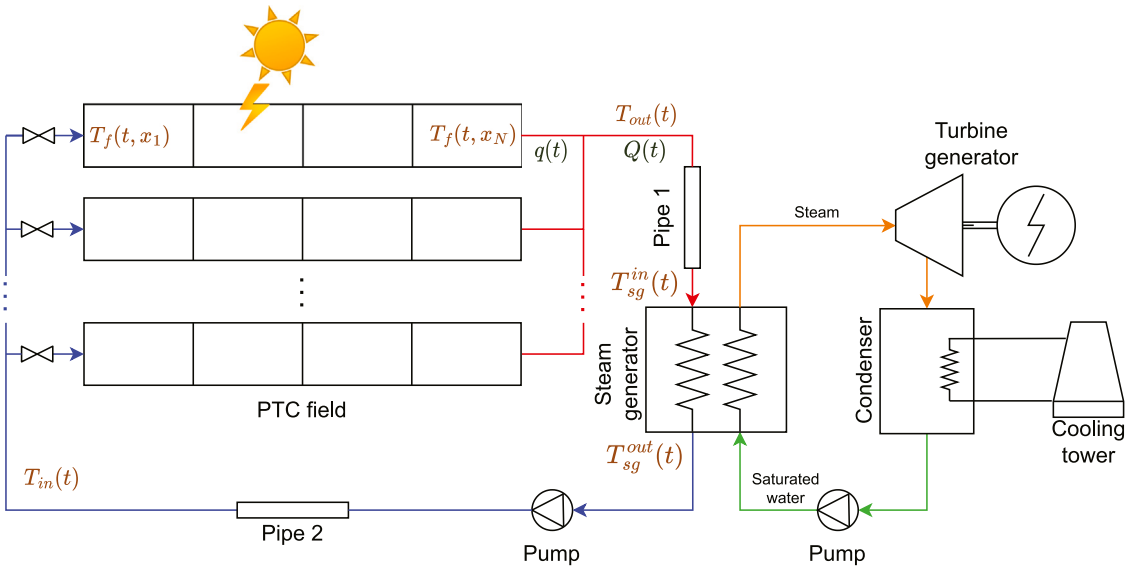


**Fig. 1.** Scheme of a parabolic-trough collector field for electric power production without thermal storage.

### 2.1. Flow-rate control

The HTF flow rate is manipulated for outlet temperature tracking. For this purpose, a feedforward controller is designed using the concentrated parameter model in steady-state, as given by Eq. (1). To compute the control signal, the non-faulty scenario is assumed (fault multipliers equal to 1).

$$q = \frac{n_o K_{opt} S I - H_l A (T_{mean} - T_a)}{P_{cp}(T_{ref} - T_{in})} \tag{1}$$

The control sample time is 30 s and the flow rate and outlet temperature constraints to protect the HTF and the components are those of Eqs. (2) and (3).

$$9\ \mathrm{m^3/h} \le q \le 33\ \mathrm{m^3/h} \tag{2}$$

$$T_{out} < 400\ ^\circ\mathrm{C} \tag{3}$$

### 2.2. Defocusing strategy

On many occasions, commercial plants need to defocus one or several collectors, i.e., to modify the angles of the collectors and take them out of focus. This way, the incidence angle between the solar beam and the normal direction to the mirror plane is augmented causing that the collector receives less energy and thus its efficiency decreases. The need to defocus the collectors is produced when the outlet temperature surpasses the maximum allowed value and the oil flow cannot be increased because of pumps or steam generator limitations, maybe due to energy constraints or to a high value of irradiance during a period of time [22].

The defocus curve shown in Fig. 2 depicts the relation between the efficiency and the defocus angle. Since this relation is not linear, it is necessary to design a defocusing mechanism that selects the angle. The work by Sánchez et al. [24], for example, proposes a method and compares the results by defocusing two and four collectors. Since the objective of this study is not the design of the defocusing mechanism, but of the FDD mechanism, a simple scheduling-based mechanism has been selected.

This paper applies a defocus strategy based on three states: solar tracking (0 °), partial defocus (2 °C) and total defocus (5 °C). Collectors 3 and 4 are allowed to achieve the three states, while collectors 1 and 2 are not allowed the second state. The defocus state is selected depending on the temperature at the center of each collector, as shown in Fig. 3. This strategy has been chosen because it is the one commonly used in commercial plants.

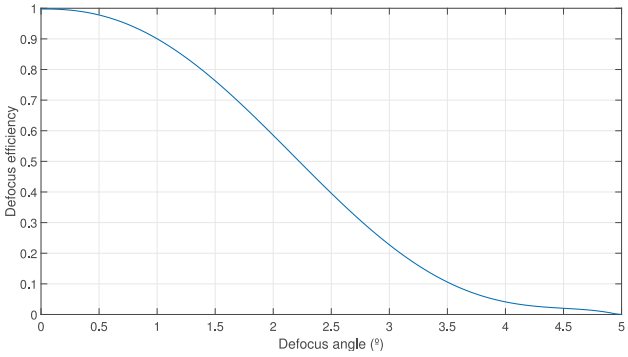


**Fig. 2.** Defocus curve.

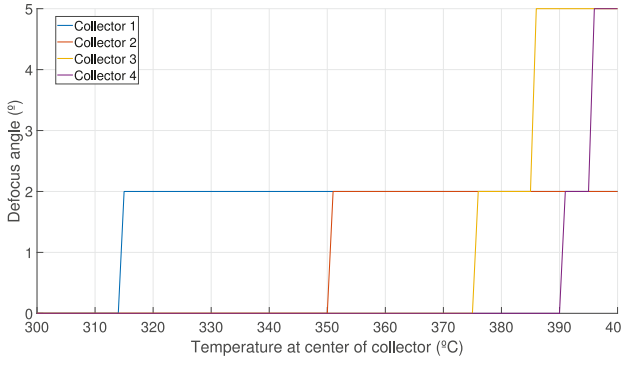


**Fig. 3.** Defocus strategy.

### 2.3. Faults considered

This work considers three types of faults in the collectors area:

- Faults in the optical efficiency, modeled as multipliers $\alpha_{K_{opt}} < 1$. The optical efficiency takes into account factors such as reflectivity and soiling of the mirrors, tube absorptance or interception factor. Within this category of faults are mirror defects, breakage, dirt, degradation, corrosion and deterioration of the tubes coating.

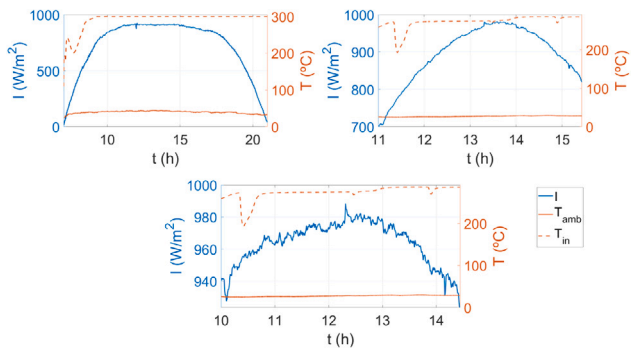


**Fig. 4.** Test profiles.

- Faults in the flow rate, modeled as $\alpha_q \neq 1$. For convenience, flow failures are introduced as additive failures that can be positive or negative, as this is more intuitive. These faults are then translated into their corresponding multiplicative factor. These faults are related to flowmeter errors and unbalances of the loops with respect to the whole plant.
- Faults in the thermal loses, modeled as $\alpha_{Hl} > 1$. These faults can be due to vacuum losses in the tubes because of the effect of dirt, wear, insulation and breakage of the pipes.

## 3. Artificial neural networks

In this work, the fault detection and classification is obtained by means of artificial neural networks, which are function approximators, specifically, multilayer perceptrons. An ANN is formed by connections of neurons organized in layers. Each neuron solves a linear regression problem and includes an activation function and its output to transform the data into an activated or non-activated state [25].

The activation functions in this work are a softmax function at the output to scale the data in the range $[0, 1]$ and hyperbolic tangent sigmoid functions at the rest of layers. The weights are trained using the scaled conjugate gradient backpropagation algorithm [26] and the architecture of the neural networks is selected by trial and error.

The inputs to the neural networks are scaled in the range $[-1, +1]$, randomized and divided into three subsets: training, validation and test sets. Additionally, new simulations with the trained neural networks are carried out to analyze their behavior in the complete system.

## 4. Methodology

The FDI methodology consists of an ANN applied in parallel with the control system with a sample time of 30 s. The inputs to the neural network are the variables of the concentrated parameter model to help it learn the dynamics of the system internally. First, a bunch of simulations is created to obtain a dataset with synthetic clear-day irradiance profiles randomly selected. Then, a dataset is created to train the neural networks using real irradiances, ambient temperatures and inlet temperatures corresponding to clear days. Finally, new simulations are carried out with new data to test the FDI system. Fig. 4 shows the profiles used for testing.

The ANNs are evaluated based on the classification accuracy (Eq. (4)) and the F1-score (Eq. (5)), where TP is rate of true positives. FP is the rate of false positives, TN is the rate of true negatives and FN is the rate of false negatives.

$$Acc = \frac{TP + TN}{TP + FP + TN + FN} \tag{4}$$

$$F1 = 2 \cdot \frac{Rec \cdot Pre}{Rec + Pre}, \quad \text{where } Pre = \frac{TP}{TP + FP} \text{ and } Rec = \frac{TP}{TP + FN} \tag{5}$$

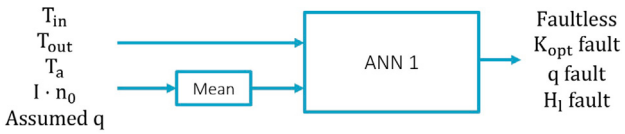


**Fig. 5.** Structure of the ANN with the first approach.

**Table 1**
Training hyperparameters of the neural networks.

| $\sigma$ | $\lambda$ | Perform. goal | Max epochs | Min gradient | Max valid. checks |
|---|---|---|---|---|---|
| $5^{-5}$ | $5^{-7}$ | 0 | $4 \cdot 10^3$ | $10^{-6}$ | 6 |

**Table 2**
Accuracies on the three subsets and training times for the ANNs of the first approach.

| ANN | Tr. Acc (%) | Val. Acc (%) | Test Acc (%) | Tr. time (h) |
|---|---|---|---|---|
| 30 | 71.4 | 71.2 | 71.3 | 1.18 |
| 30–20 | 84.0 | 83.9 | 83.9 | 1.85 |
| 30–20–8 | 79.0 | 78.9 | 78.9 | 2.09 |
| 60–30 | 89.2 | 89.1 | 89.2 | 3.03 |
| 60–30–12 | 89.1 | 89.1 | 89.0 | 3.45 |
| 120–60 | 93.7 | 93.6 | 93.7 | 5.37 |
| 120–60–20 | 92.3 | 92.2 | 92.2 | 6.13 |
| 350–180 | 96.7 | 96.7 | 96.7 | 15.5 |

### 4.1. First approach: Without defocusing information

The first approach consists of analyzing the ability of multilayer perceptrons to detect and isolate the three types of faults without knowing information about the defocusing strategy, as in [20]. The structure of the ANN is shown in Fig. 5.

Specifically, the inputs to ANN 1 are $X(k) = [T_{in}(k), \mu_{T_{in}}(k-5 : k-1), \mu_{T_{in}}(k-20 : k-6), T_{out}(k), \mu_{T_{out}}(k-5 : k-1), \mu_{T_{out}}(k-15 : k-6), \mu_{T_{out}}(k-30 : k-16), T_a(k), I(k)n_o(k), \mu_{In_0}(k-5 : k-1), \mu_{In_0}(k-20 : k-6), q(k), \mu_q(k-3 : k-1), \mu_q(k-10 : k-4)]$, where $\mu$ denotes the average value.

A dataset of 1487360 instances (2688 days) was created to train the ANNs. The data corresponds to different simulations with and without faults between 10:00 h and 17:59 h. The reference temperatures for the controller were randomly chosen between 369 °C and 390 °C, and the maximum irradiance values were also randomly selected between 750 W/m$^2$ and 1000 W/m$^2$. The faults in these first experiments are in the following ranges: $\alpha_{K_{opt}} \in [0.1, 0.9]$ for the optical efficiency faults, $\delta_q \in [\pm 1.65, \pm 3.3]$ m$^3$/h for the flow rate additive faults and $\alpha_{H_l} \in [1.1, 2]$ for the thermal losses faults.

The neural networks were trained with the hyperparameters of Table 1.

Table 2 shows the accuracies of the trained neural networks in the three subsets. The column ANN indicates the number of neurons in each layer. All deep architectures (the ones with more than one hidden layer) perform well and there is a low overfitting, judging from the accuracy evolution between subsets. The results show that the addition of a third hidden layer worsens the accuracy.

To reduce false alarms during a day, the output of the ANN is filtered with a certain time constant and, whenever one output corresponding to a fault surpass a certain threshold, an alarm is triggered. 384 simulations of one day were performed using the test profiles of Fig. 4 for three selected neural network with different thresholds and filter time constants. The results are gathered in Table 3. The highest accuracies are over 70%. They are achieved with the ANN of 120 and 60 neurons with a limit of 50% and the ANN of 30 and 20 neurons with a limit of 75%, both with a 90 min filter.

**Table 3**
Simulation results of the first FDD approach with the selected neural networks.

| ANN | Threshold, filter | Faultless | F1-score (%) | | | Acc. |
|---|---|---|---|---|---|---|
| | | | $K_{opt}$ fault | $q$ fault | $H_l$ fault | (%) |
| 30–20 | 0.5, 60 | 46.6 | 66.1 | 53.9 | 50.5 | 53.4 |
| 120–60 | 0.5, 60 | 49.0 | 67.7 | 61.4 | 40.9 | 52.1 |
| 350–180 | 0.5, 60 | 47.5 | 81.5 | 59.6 | 54.2 | 61.2 |
| 30–20 | 0.5, 90 | 59.3 | 65.7 | 51.5 | 54.9 | 57.6 |
| 120–60 | 0.5, 90 | 76.2 | 80.3 | 69.0 | 64.4 | 71.7 |
| 350–180 | 0.5, 90 | 37.5 | 81.3 | 43.5 | 46.7 | 51.5 |
| 30–20 | 0.75, 90 | 78.7 | 81.0 | 67.4 | 60.3 | 71.7 |
| 120–60 | 0.75, 90 | 73.7 | 79.1 | 65.0 | 60.1 | 68.8 |
| 350–180 | 0.75, 90 | 71.3 | 92.1 | 49.0 | 58.4 | 69.4 |

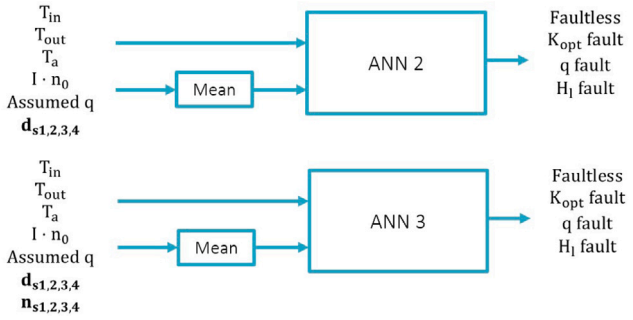


**Fig. 6.** Structure of the ANNs with the second approach.

**Table 4**
Accuracies on the three subsets and training times for the ANNs of the second approach.

| ANN | Tr. Acc (%) | Val. Acc (%) | Test Acc (%) | Tr. time (h) |
|---|---|---|---|---|
| ANN 2: | | | | |
| 30–20 | 89.0 | 89.1 | 89.0 | 1.97 |
| 120–60 | 97.9 | 97.7 | 97.7 | 5.64 |
| 350–180 | 99.2 | 99.0 | 99.0 | 11.2 |
| ANN 3: | | | | |
| 30–20 | 89.9 | 89.9 | 89.9 | 1.57 |
| 120–60 | 95.1 | 95.0 | 94.9 | 5.97 |
| 350–180 | 99.4 | 99.2 | 99.2 | 15.1 |

### 4.2. Second approach: With defocusing information

The second approach involves taking into account the defocusing information. For this purpose, two new variables are created: the defocusing state $s_{di}$ and the number of defocusings in a time period $n_{di}$ for each collector $i$. The ANN structures used in this approach are shown in Fig. 6.

This way, the inputs for ANN 2 are $X(k) = [T_{in}(k)$, $\mu_{T_{in}}(k-5:k-1)$, $\mu_{T_{in}}(k-20:k-6)$, $T_{out}(k)$, $\mu_{T_{out}}(k-5:k-1)$, $\mu_{T_{out}}(k-15:k-6)$, $\mu_{T_{out}}(k-30:k-16)$, $T_a(k)$, $I(k)n_o(k)$, $\mu_{In_0}(k-5:k-1)$, $\mu_{In_0}(k-20:k-6)$, $q(k)$, $\mu_q(k-3:k-1)$, $\mu_q(k-10:k-4)$, $s_{d1}(k)$, $s_{d2}(k)$, $s_{d3}(k)$, $s_{d4}(k)$, $\mu_{s_{d1}}(k-60:k)$, $\mu_{s_{d2}}(k-60:k)$, $\mu_{s_{d3}}(k-60:k)$, $\mu_{s_{d4}}(k-60:k)]$, and for ANN 3 are $X(k) = [T_{in}(k)$, $\mu_{T_{in}}(k-5:k-1)$, $\mu_{T_{in}}(k-20:k-6)$, $T_{out}(k)$, $\mu_{T_{out}}(k-5:k-1)$, $\mu_{T_{out}}(k-15:k-6)$, $\mu_{T_{out}}(k-30:k-16)$, $T_a(k)$, $I(k)n_o(k)$, $\mu_{In_0}(k-5:k-1)$, $\mu_{In_0}(k-20:k-6)$, $q(k)$, $\mu_q(k-3:k-1)$, $\mu_q(k-10:k-4)$, $s_{d1}(k)$, $s_{d2}(k)$, $s_{d3}(k)$, $s_{d4}(k)$, $\mu_{s_{d1}}(k-60:k)$, $\mu_{s_{d2}}(k-60:k)$, $\mu_{s_{d3}}(k-60:k)$, $\mu_{s_{d4}}(k-60:k)$, $\sum n_{d1}(k-60:k)$, $\sum n_{d2}(k-60:k)$, $\sum n_{d3}(k-60:k)$, $\sum n_{d4}(k-60:k)]$.

A new dataset is created again and neural networks are trained with the same characteristics as the three selected from the previous experiment, but with different the inputs. The accuracies in the three subsets are those of Table 4. The accuracies with this second approach are higher that with the first approach.

**Table 5**
Simulation results of the second FDD approach with the selected neural networks.

| ANN | Threshold, filter | Faultless | F1-score (%) | | | Acc. |
|---|---|---|---|---|---|---|
| | | | $K_{opt}$ fault | $q$ fault | $H_l$ fault | (%) |
| ANN 2: | | | | | | |
| 30–20 | 0.5, 60 | 90.7 | 85.9 | 64.2 | 60.1 | 75.5 |
| 120–60 | 0.5, 60 | 75.3 | 81.8 | 46.9 | 74.9 | 69.3 |
| 350–180 | 0.5, 60 | 72.2 | 83.4 | 70.4 | 50.0 | 68.3 |
| 30–20 | 0.5, 90 | 87.3 | 94.4 | 63.4 | 60.6 | 77.4 |
| 120–60 | 0.5, 90 | 75.9 | 82.3 | 38.1 | 56.9 | 62.1 |
| 350–180 | 0.5, 90 | 64.0 | 83.5 | 64.4 | 47.2 | 63.3 |
| 30–20 | 0.75, 90 | 84.2 | 91.9 | 62.6 | 44.7 | 72.9 |
| 120–60 | 0.75, 90 | 74.4 | 82.8 | 40.5 | 54.8 | 62.3 |
| 350–180 | 0.75, 90 | 80.2 | 90.1 | 68.2 | 57.1 | 74.7 |
| ANN 3: | | | | | | |
| 30–20 | 0.5, 60 | 93.5 | 96.7 | 69.1 | 70.1 | 84.0 |
| 120–60 | 0.5, 60 | 77.6 | 81.6 | 47.0 | 63.1 | 67.2 |
| 350–180 | 0.5, 60 | 49.548 | 76.4 | 58.2 | 55.9 | 60.0 |
| 30–20 | 0.5, 90 | 85.1 | 97.3 | 68.2 | 68.2 | 81.0 |
| 120–60 | 0.5, 90 | 70.1 | 85.4 | 45.3 | 51.5 | 63.7 |
| 350–180 | 0.5, 90 | 49.5 | 75.6 | 50.8 | 49.5 | 55.3 |
| 30–20 | 0.75, 90 | 84.2 | 94.0 | 73.3 | 64.0 | 80.0 |
| 120–60 | 0.75, 90 | 67.1 | 87.8 | 47.0 | 49.2 | 64.4 |
| 350–180 | 0.75, 90 | 46.3 | 76.9 | 48.3 | 46.7 | 53.4 |

As shown in Table 5, the best accuracies are around 10% better than without the defocusing information, with F1-scores in the non-faulty output and the $K_{opt}$ fault over 90%, and the best ANNs need less neurons. The highest accuracies and F1-scores with ANN 3 are obtained with the neural network of 30 and 20 neurons and with the one of 350 and 180 neurons for ANN 2, and with the one with 30 and 20 neurons for ANN 3.

### 4.3. Third approach: Selecting range of faults

One question that arises during the training process is about the goodness of the considered range of faults, as it is designed to cover a wide space that may not be realistic and not take into account the real effect of the faults on the plant. Moreover, the analysis of the ANNs accuracies does not take into account the ability of the ANNs to classify each fault size. For this reason, this work proposes to create a new fault range based on these aspects.

The first analysis focuses on the hit rate for each fault rate, measured with the specific recall. This metric takes the number of test simulations performed for each fault size and keeps track of the rate of correct classifications. It is computed for a subset of the simulations with a specific value of fault multiplier as in Eq. (6), where $TP\alpha_i$ is the number of correctly detected faults of a specific value of one fault multiplier $\alpha_i$ and $FN\alpha_i$ is the number of non-detected faults of that type and size.

$$Rec(\alpha_i) = \frac{TP_{\alpha_i}}{TP_{\alpha} + FN_{\alpha_i}} \tag{6}$$

Subsequently, the average of the recall values for every fault type and size among the best trained ANNs is obtained and a curve is generated by cubic interpolation as in Fig. 7. This curve will be used to select the new range of faults.

When deciding whether a failure is important or not, it is necessary to know its effect on the system. The next step is to analyze the effect of each fault on the outlet temperature. For this purpose, different simulations under the same circumstances, but with and without faults, are compared. The percentage temperature drop is shown in Fig. 8 as blue crosses, together with the mean values $\mu$. Then, according with to $3\sigma$ rule – which states that 99.7% of the observed data following a normal distribution are within 3 standard deviation of the mean –, a curve is obtained to represent the 3 standard deviation over the mean to cover a wide range. This curve is combined with the previous curve obtaining the yellow one, which finally takes into account not only the

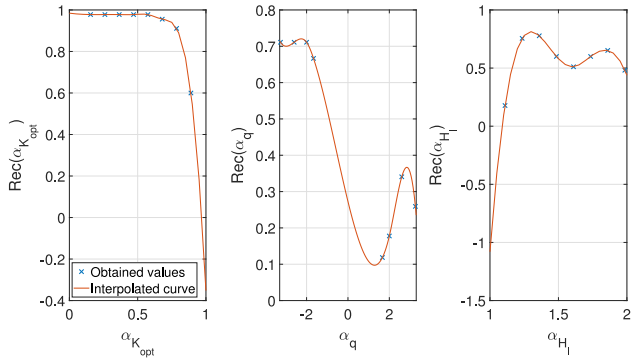


**Fig. 7.** Average recalls and curves obtained.

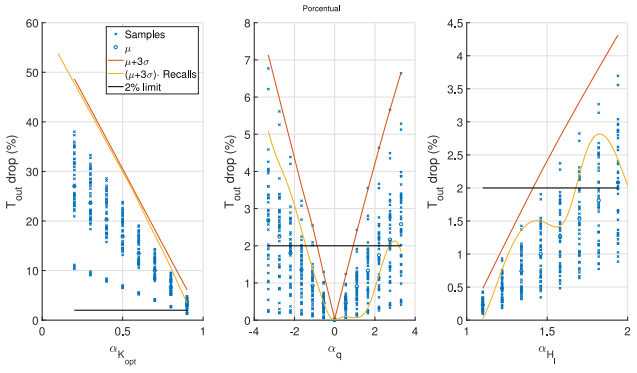


**Fig. 8.** Effect on the output of each fault and curves obtained. (For interpretation of the references to color in this figure legend, the reader is referred to the web version of this article.)

**Table 6**
Accuracies on the three subsets and training times for the ANNs of the third approach.

| ANN | Tr. Acc (%) | Val. Acc (%) | Test Acc (%) | Tr. time (h) |
|---|---|---|---|---|
| ANN 2: | | | | |
| 30–20 | 93.8 | 93.8 | 93.8 | 1.26 |
| 350–180 | 99.4 | 99.4 | 99.3 | 15.3 |
| ANN 3: | | | | |
| 30–20 | 93.9 | 93.9 | 93.9 | 1.21 |

ability of the ANNs to detect each fault, but also the effect on the outlet temperature.

The new ranges of faults are selected according to whether the curve surpasses the 2% or not. This way, whenever the curve is lower than 2%, the fault is considered unimportant and is taken out of the fault range. The new values of the multipliers are $\alpha_{K_{opt}} \in [0.1, 0.9]$, $\alpha_q \in [-3.3, -1.5] \cup [2.6, 3.3]$ and $\alpha_{H_l} \in [1.67, 2]$. With these new fault values, another dataset is created with the same characteristics as the previous ones, and ANNs with the same hyperparameters and inputs are trained. The architectures selected were the ones with the highest accuracies in the second approach. The accuracies in the three subsets and training times are shown in Table 6. The training results are slightly better than with the second approach and the accuracies do not differ between subsets.

As observed in Table 7, the accuracies and F1-scores are much better, obtaining values around 90% for all the classes with the ANN of type 3 that contains 30 neurons in the first hidden layer and 20 neurons in the second one, with a limit of 75% and a 90 min filter. The filter time constants and output thresholds for each ANN architecture are selected to be the same as in the second approach. The F1-scores and accuracies surpass those of the previous approaches.

**Table 7**
Simulation results of the third FDD approach with the selected neural networks.

| ANN | Threshold, filter | Faultless | F1-score (%) $K_{opt}$ fault | $q$ fault | $H_l$ fault | Acc. (%) |
|---|---|---|---|---|---|---|
| ANN 2: | | | | | | |
| 30–20 | 0.5, 60 | 96 | 95.65 | 64.22 | 68.7 | 79.63 |
| 350–180 | 0.5, 60 | 98.97 | 96.77 | 58.79 | 48.17 | 73.3 |
| 30–20 | 0.5, 90 | 89.72 | 93.73 | 80.48 | 77.67 | 85.42 |
| 350–180 | 0.5, 90 | 96 | 95.65 | 73.58 | 65.12 | 82.81 |
| 30–20 | 0.75, 90 | 89.72 | 93.33 | 89.13 | 82.11 | 88.54 |
| 350–180 | 0.75, 90 | 95.68 | 95.65 | 79.41 | 79.21 | 87.5 |
| ANN 3: | | | | | | |
| 30–20 | 0.5, 60 | 85.71 | 88.66 | 76.47 | 69.52 | 79.48 |
| 30–20 | 0.5, 90 | 90.57 | 94.51 | 77.73 | 77.71 | 85.24 |
| 30–20 | 0.75, 90 | 90.57 | 93.33 | 92.13 | 86.87 | 90.62 |

**Table 8**
Best results for each approach.

| Method | F1-score (%) Faultless | $K_{opt}$ fault | $q$ fault | $H_l$ fault | Acc (%) |
|---|---|---|---|---|---|
| Without defocusing inputs | 76.19 | 80.31 | 69.00 | 64.43 | 71.72 |
| With defocusing inputs | 93.51 | 96.73 | 69.14 | 70.12 | 83.96 |
| New ranges | 90.57 | 93.33 | 92.13 | 86.87 | 90.62 |

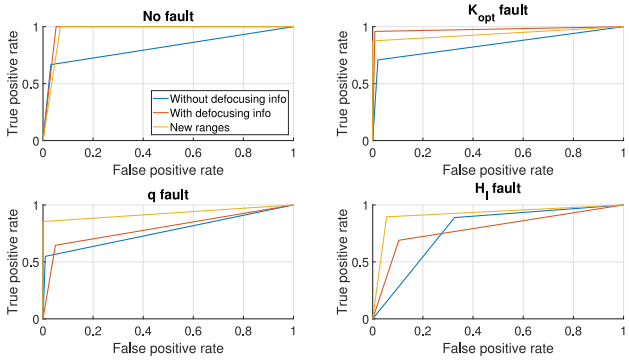


**Fig. 9.** ROC curves for each fault class.

## 5. Summary of the results and discussion

This work has addressed three approaches for FDI in a PTC plant with a defocusing strategy. Table 8 collects the best results for each approach based on the accuracy and F1-scores. These results demonstrate that adding inputs to the ANNs that contain defocusing data can lead to more than a 10% better accuracy and F1-scores over 90% in the faultless and the optical efficiency fault cases. This means that the neural networks can distinguish better between an optical efficiency fault and a defocusing mode, and that the defocusings help the ANNs decouple the faults more effectively. This way, the ANNs can internally model the dynamics of the plant.

The Receiver operating characteristic (ROC) [27] curve provides a visual representation of the true and false positive rates and is shown in Fig. 9 for each one of the fault classes. The area under the curve (AUC) for the non-faulty class is 81.77%, 97.40% and 96.53% for the ANN without defocusing information, the one with defocusing information and the one with new ranges, respectively. The AUCs for the optical efficiency faults are 84.38%, 97.48% and 93.75%, the AUCs for the flow rate faults are 76.97%, 79.83% and 92.71%, and the AUCs for the thermal losses faults are 28.13%, 79.28% and 92.01%.

When there is a plant in which there are flow rate changes and defocuses and the neural networks are provided with information about the defocus and the time evolution, it is allowed to analyze the failures in a way similar to the strategy performed in [13], but in an automatic

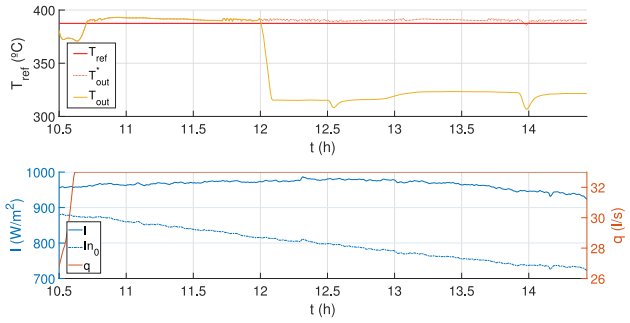


**Fig. 10.** Temperature, irradiance and flow rate with $\alpha_{K_{opt}} = 0.35$ at 12:00.

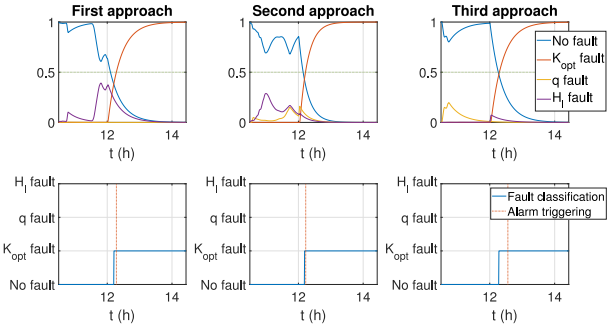


**Fig. 11.** Fault classification of the three approaches with $\alpha_{K_{opt}} = 0.35$ at 12:00.

way. This is due to the fact that when the collectors are decoupled and the FDD system is aware of it, if the plant does not behave as expected, there is definitely a failure in the flow rate or the thermal loses. If changes in input are also introduced and the ANN knows the inlet and outlet temperature for several sampling times, the ANN is given the ability to internally extrapolate flow residence times. This information is of great help in detecting flow failures. If no flow failures are found and the system is not behaving correctly, it is more likely to be a thermal losses failure.

On the other hand, the analyzable ranges of faults have been modified and an improvement of almost 90% has been obtained, with F1-scores close to 90% in all classes. This means that ANN is able to detect both positives and negatives in approximately the same way for all classes. Depending on the fault detection objectives, the second or third approach will be more suitable. The first approach covers a larger range of faults with lower accuracy, and the second approach covers a smaller range of more important faults with higher accuracy.

The results of the ANNs selected for each approach with the test profiles are shown below. Fig. 10 shows the temperature, flow rate and irradiance of a day with a fault of $\alpha_{K_{opt}} = 0.35$ in the optical efficiency occurring at 12:00. $T^*_{out}$ is the value of the outlet temperature if there is no fault. As shown in Fig. 11, the selected neural networks for the three approaches obtain a good classification of the fault.

Fig. 12 shows the temperature, flow rate and irradiance conditions of a test were a flow rate fault of $\delta_q = 3.1$ was introduced at 13:00. The classifications are shown in Fig. 13. A case has been shown in which all three approaches manage to detect the fault well, although with greater difficulty.

Finally, the temperature, flow rate and irradiance of a test with a thermal loses fault of $\alpha_{H_l} = 1.835$ at 11:30 is shown in Fig. 14. Fig. 15 shows the classification results. In this case, only the ANNs of the first and third approach could detect the faults correctly.

For obtaining the F1-scores and accuracies, simulations of 792 days were used with an even split between the three profiles and fault sizes. Table 9 gathers the 95% confidence intervals values of the accuracies

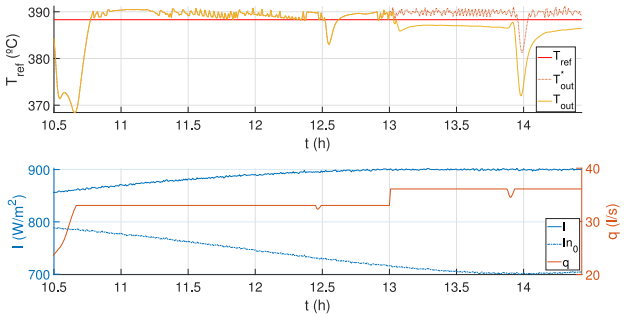


**Fig. 12.** Temperature, irradiance and flow rate with $\delta_q = 3.1$ at 13:00.

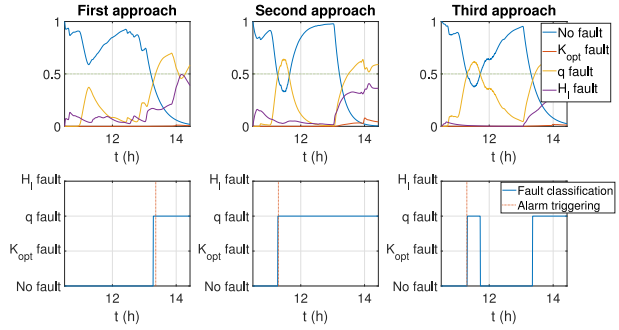


**Fig. 13.** Fault classification of the three approaches with $\delta_q = 3.1$ at 13:00.

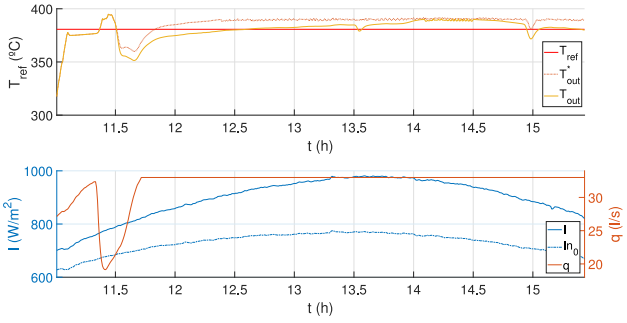


**Fig. 14.** Temperature, irradiance and flow rate with $\alpha_{H_l} = 1.835$ at 11:30.

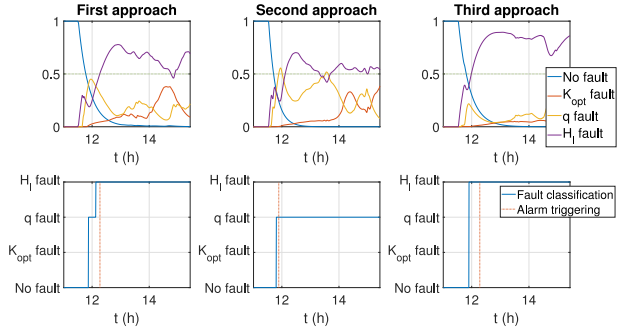


**Fig. 15.** Fault classification of the three approaches with $\alpha_{H_l} = 1.835$ at 11:30.

and F1-scores of the selected neural networks after performing several tests formed by different numbers of days, from 300 to 2100, with random faults and parameters. Assuming a normal distribution, the confidence intervals are defined as $(\bar{x} - c\frac{\sigma}{\sqrt{n}}, \bar{x} + c\frac{\sigma}{\sqrt{n}})$, where $\bar{x}$ is the mean, $c$ is the selected percentile, $\sigma$ is the standard deviation and $n$ is the sample size.

**Table 9**
95% Confidence intervals of the evaluation metrics the selected methods.

| Method | F1-score (%) | | | | Acc |
|---|---|---|---|---|---|
| | Faultless | $K_{opt}$ fault | $q$ fault | $H_l$ fault | (%) |
| Without defocusing info | (79.4, 84.66) | (78.39, 84.41) | (49.59, 59.68) | (57.98, 62.62) | (66.28, 70.9) |
| With defocusing info | (96.36, 97.93) | (95.65, 97.54) | (65.27, 69.64) | (65.3, 70.11) | (81.03, 83.56) |
| New ranges | (91.28, 93.9) | (91.04, 92.62) | (88.62, 93.12) | (82.57, 85.28) | (89.1, 90.88) |

## 6. Conclusions and future work

This work has presented three steps for fault detection and diagnosis in a 50 MW plant of parabolic trough collectors that has a defocusing strategy. The proposed methods are based on the use of multi-label classification neural networks and are trained and tested on sunny days, where the plant variables are more stable than in days with great clouds.

The results are supported by simulation tests that prove that adding information about the defocusing state and the number of defocusings in a time window improve the performance of the ANNs. Likewise, the results can be improved to around 90% when adjusting the fault ranges to ones that combine the detectability of the faults and their influence to the plant output.

Future lines of development include the application of these methods to other plants, determining the magnitude of the detected faults, and generalizing the approach to the entire field, including faults outside the collector area. Moreover, the possibility of testing the method in real plants is being considered.

## Declaration of competing interest

The authors declare that they have no known competing financial interests or personal relationships that could have appeared to influence the work reported in this paper.

## Acknowledgment

This research has received funding from the European Research Council (ERC) under the European Union's Horizon 2020 research and innovation programme (OCONTSOLAR, grant agreement No 789051) and the Spanish Ministry of Science, Innovation, and Universities (Grant FPU20/01958).

## Appendix. Physical plant model

### A.1. Dynamic model of a loop

The methodology described in this work is applied to one collector loop, since the procedure can be implemented collector by collector, and is extensible to the entire plant. The dynamic model of a collector loop is presented below. The system is described with the distributed parameter model given by Eqs. (A.1) and (A.2), which represent the energy balances in the fluid and the pipe using spatially distributed variables [28,29]. It is a well-known model validated by Camacho et al. [30] that has been used by researchers in many different studies such as the works by Masero et al. [31], and Gholaminejad and Khaki-Sedigh [32].

The dimensions of the reflector and receiver are presumed to be equal along the active part of the loop. For this reason, a uniform local concentration ratio is assumed. The temperature of the metal is assumed to be radially constant. To compute the equations, the loop is discretized into 151 segments of 3.213 m. The integration time is 0.25 s.

The equations include three multipliers, each one corresponding to one type of fault: faults in the optical efficiency $\alpha_{K_{opt}}$, faults in the flow rate $\alpha_q$ and faults in the thermal losses $\alpha_{Hl}$.

$$\rho_m C_m A_m \frac{\partial T_m}{\partial t} = \alpha_{K_{opt}} I K_{opt} eff_{def} n_o G + \\ -H_l G(T_m - T_a) - LH_t(T_m - T_f) \tag{A.1}$$

$$\rho_f C_f A_f \frac{\partial T_f}{\partial t} + \alpha_q \rho_f C_f q \frac{\partial T_f}{\partial x} = LH_t(T_m - T_f) \tag{A.2}$$

The density $\rho_f$ and specific heat capacity $C_f$ of the Therminol VP-1 HTF are given by Eqs. (A.3) and (A.4) [33].

$$\rho_f = -4.810 \cdot 10^{-4} T_f^2 - 8.110 \cdot 10^{-1} T_f + 9.537 \cdot 10^2 \tag{A.3}$$

$$C_f = 1.561 \cdot 10^{-8} T_f^2 + 1.707 \cdot 10^{-1} T_f + 1.574 \cdot 10^2 \tag{A.4}$$

The rest of the parameters are as follows. The pipe steel is DIN 1.4404, with density $\rho_m = 7800$ kg/m$^3$ and specific heat capacity $C_m = 550$ J/Kg° C. The cross-sectional areas are $A_m = 2.1677 \cdot 10^{-4}$ m$^2$ and $A_f = 3.6 \cdot 10^{-3}$ m$^2$. The collector aperture is $G = 5.75$ m and the tube internal perimeter is $2.136 \cdot 10^{-1}$ m. The thermal loss coefficient and the coefficient of convective heat transfer are given by Eqs. (A.5) and (A.6). These parameters were obtained from the Mojave Beta Solar Plant. This is an actual solar trough plant which produces up to 140 MW of electrical power [33].

$$H_l = 1.137 \cdot 10^{-8} \left(T_f - T_a\right)^3 - 3.235 \cdot 10^{-6} \left(T_f - T_a\right)^2 + \\ +1.444 \cdot 10^{-4} \left(T_f - T_a\right) + 8.179 \cdot 10^{-2} - \frac{4.796}{\left(T_f - T_a\right)} \tag{A.5}$$

$$H_t = \frac{q}{3600}^{0.818} (-3.243 \cdot 10^{-4} T_f^3 + 2.442 \cdot 10^{-1} T_f^2 + \\ +2.320 \cdot 10^2 T_f + 2.532 \cdot 10^4) \tag{A.6}$$

The geometric efficiency is known as $n_o$ or $cos(\theta)$. It is a factor that depends on the collector dimensions, solar hour, hourly angle, declination, latitude and Julian day and is computed by means of the relation between the radiation beam vector and the normal vector of the mirror [34]. Given that this plant is north–south aligned, the geometric efficiency is computed as in Eq. (A.7) [35].

$$n_0 = \left((\sin(\phi)\sin(\delta_s) + \cos(\phi)\cos(\delta_s)\cos(\omega_s))^2 + \right. \\ \left. + \cos^2(\delta_s)\sin^2(\omega_s)\right)^{\frac{1}{2}} \tag{A.7}$$

### A.2. Concentrated parameter model

To control the plant, a simpler description of the model was used. The concentrated parameter model – or lumped parameter model – describes the internal energy variation of the HTF and is given by Eq. (A.8). This model is well known and has been extensively used in the literature. Examples of this are the works by Sánchez-Amores et al. [36] and Velarde et al. [37]. In this work, the model was used for design purposes: to develop a feedforward controller and to select the inputs to the neural network.

$$C_{loop} \frac{dT_{out}}{dt} = -\alpha_q q P_{cp}(T_{out} - T_{in}) - \alpha_{H_l} H_l A(T_{mean} - T_a) + \\ +\alpha_{K_{opt}} n_o K_{opt} SI \tag{A.8}$$

with the loop thermal capacity given by the expression $C_{loop} = L_{loop}\rho_m C_m A_f$ and $P_{cp} = \rho_m C_m$.

## References


[1] S. Suman, Hybrid nuclear-renewable energy systems: A review, J. Clean. Prod. 181 (2018) 166–177, http://dx.doi.org/10.1016/j.jclepro.2018.01.262.

[2] A. Azam, M. Rafiq, M. Shafique, H. Zhang, J. Yuan, Analyzing the effect of natural gas, nuclear energy and renewable energy on GDP and carbon emissions: A multi-variate panel data analysis, Energy 219 (2021) 119–592, http://dx.doi.org/10.1016/j.energy.2020.119592.

[3] Z. Şen, Solar energy in progress and future research trends, Prog. Energy Combust. Sci. 30 (2004) 367–416, http://dx.doi.org/10.1016/j.pecs.2004.02.004.

[4] W. Ajbar, A. Parrales, A. Huicochea, J.A. Hernández, Different ways to improve parabolic trough solar collectors' performance over the last four decades and their applications: A comprehensive review, Renew. Sustain. Energy Rev. 156 (2022) 111947, http://dx.doi.org/10.1016/j.rser.2021.111947.

[5] A. Untrau, S. Sochard, F. Marias, J.-M. Reneaume, G.A.C.L. Roux, S. Serra, Analysis and future perspectives for the application of dynamic real-time optimization to solar thermal plants: A review, Sol. Energy 241 (2022) 275–291, http://dx.doi.org/10.1016/j.solener.2022.05.058.

[6] A.F. Branco, M.M. Morato, G.A. Andrade, J.E. Normey-Rico, Tools for the control of modern solar-thermal heating plants, in: Proceedings of the 14th Brazilian Symposium of Inteligent Automation (SBAI), Ouro Preto, Brazil, Oct. 27-30, 2019, Vol. 1, 2019, 104234, http://dx.doi.org/10.17648/sbai-2019-111095.

[7] D. Miljković, Fault detection methods: A literature survey, in: 2011 Proceedings of the 34th international convention MIPRO, 2011, pp. 750–755.

[8] V. Venkatasubramanian, R. Rengaswamy, K. Yin, S.N. Kavuri, A review of process fault detection and diagnosis: Part I: Quantitative model-based methods, Comput. Chem. Eng. 27 (2003) 293–311, http://dx.doi.org/10.1016/S0098-1354(02)00160-6.

[9] G. Faure, M. Vallée, C. Paulus, T. Tran, Fault detection and diagnosis for large solar thermal systems: A review of fault types and applicable methods, Sol. Energy 197 (2020) 472–484, http://dx.doi.org/10.1016/j.solener.2020.01.027.

[10] Z. He, P. Chu, C. Li, K. Zhang, H. Wei, Y. Hu, Compound fault diagnosis for photovoltaic arrays based on multi-label learning considering multiple faults coupling, Energy Convers. Manage. 279 (2023) 116742, http://dx.doi.org/10.1016/j.enconman.2023.116742.

[11] S. Bououden, F. Allouani, A. Abboudi, M. Chadli, I. Boulkaibet, Z.A. Barakeh, B. Neji, R. Ghandour, Observer-based robust fault predictive control for wind turbine time-delay systems with sensor and actuator faults, Energies 16 (2023) 858, http://dx.doi.org/10.3390/en16020858.

[12] A. Zafra-Cabeza, J.J. Marquez, C. Bordons, M.A. Ridao, An online stochastic MPC-based fault-tolerant optimization for microgrids, Control Eng. Pract. 130 (2023) 105381, http://dx.doi.org/10.1016/j.conengprac.2022.105381.

[13] S. Ruiz-Moreno, A. Sanchez, A. Gallego, E. Camacho, A deep learning-based strategy for fault detection and isolation in parabolic-trough collectors, Renew. Energy 186 (2022) http://dx.doi.org/10.1016/j.renene.2022.01.029.

[14] F. Rodríguez, W.D. Chicaiza, A.J. Sánchez, J.M. Escaño, Neural networks techniques for fault detection and offset prediction on wind turbines sensors, in: International Workshop on Soft Computing Models in Industrial and Environmental Applications, 2023, pp. 534–543, http://dx.doi.org/10.1007/978-3-031-18050-7_52.

[15] M. Ahmadipour, M.M. Othman, R. Bo, Z. Salam, H.M. Ridha, K. Hasan, A novel microgrid fault detection and classification method using maximal overlap discrete wavelet packet transform and an augmented Lagrangian particle swarm optimization-support vector machine, Energy Rep. 8 (2022) 4854–4870, http://dx.doi.org/10.1016/j.egyr.2022.03.174.

[16] C. Correa-Jullian, J.M. Cardemil, E.L. Droguett, M. Behzad, Assessment of deep learning algorithms for fault diagnosis in solar thermal systems, in: ISES Solar World Congress, Vol. 2019, 2019, http://dx.doi.org/10.18086/swc.2019.08.03.

[17] S. Jiang, M. Lian, C. Lu, S. Ruan, Z. Wang, B. Chen, {SVM-DS} fusion based soft fault detection and diagnosis in solar water heaters, Energy Explor. Exploitation 37 (2019) 1125–1146, http://dx.doi.org/10.1177/0144598718816604.

[18] C. Schmelzer, M. Georgii, J. Orozaliev, K. Vajen, Fault detection for solar thermal systems–overall system evaluation or component-oriented approach, in: Proceedings of the ISES EuroSun 2020 Conference–13th International Conference on Solar Energy for Buildings and Industry. Presented at the EuroSun 2020, 2020, pp. 1–8, http://dx.doi.org/10.18086/eurosun.2020.04.02A.

[19] A. Brenner, T. Hirsch, M. Röger, R. Pitz-Paal, Condition monitoring for parabolic trough fields–soiling determination, in: SFERA-III 2nd Doctoral Colloquium-Book of abstracts, Vol. 129, 2021.

[20] S. Ruiz-Moreno, A. Gallego, A. Sanchez, E. Camacho, Deep learning-based fault detection and isolation in solar plants for highly dynamic days, in: 2022 International Conference on Control, Automation and Diagnosis, ICCAD 2022, 2022, http://dx.doi.org/10.1109/ICCAD55197.2022.9853987.

[21] S. Ruiz-Moreno, A.J. Gallego, A.J. Sanchez, E.F. Camacho, A cascade neural network methodology for fault detection and diagnosis in solar thermal plants, Renew. Energy (2023) http://dx.doi.org/10.1016/j.renene.2023.04.051.

[22] A.J. Sánchez, A.J. Gallego, J.M. Escaño, E.F. Camacho, Event-based MPC for defocusing and power production of a parabolic trough plant under power limitation, Sol. Energy 174 (2018) 570–581, http://dx.doi.org/10.1016/j.solener.2018.09.044.

[23] Therminol VP1 HTF, 2023, URL https://www.therminol.com/product/71093459?pn=Therminol-VP-1-Heat-Transfer-Fluid.

[24] A.J. Sánchez, A.J. Gallego, J.M. Escaño, E.F. Camacho, Parabolic trough collector defocusing analysis: Two control stages vs four control stages, Sol. Energy 209 (2020) 30–41, http://dx.doi.org/10.1016/j.solener.2020.09.001.

[25] P. Ramachandran, B. Zoph, Q.V. Le, Searching for activation functions, 2017, http://dx.doi.org/10.48550/arXiv.1710.05941, arXiv preprint arXiv:1710.05941.

[26] M.F. Møller, A scaled conjugate gradient algorithm for fast supervised learning, Neural Netw. 6 (1993) 525–533.

[27] T. Fawcett, ROC graphs: Notes and practical considerations for researchers, Mach. Learn. 31 (1) (2004) 1–38.

[28] R. Carmona, Analisis, modelado y control de un campo de colectores solares distribuidos con sistema de seguimiento en un eje, University of Seville, Spain, 1985.

[29] E.F. Camacho, M. Berenguel, F.R. Rubio, Advanced Control of Solar Plants, Springer, 1997, http://dx.doi.org/10.1007/978-1-4471-0981-5.

[30] E.F. Camacho, M. Berenguel, F.R. Rubio, D. Martinez, Control of Solar Energy Systems, Springer-Verlag, 2012, http://dx.doi.org/10.1007/978-0-85729-916-1.

[31] E. Masero, J.R.D. Frejo, J.M. Maestre, E.F. Camacho, A light clustering model predictive control approach to maximize thermal power in solar parabolic-trough plants, Sol. Energy 214 (2021) 531–541, http://dx.doi.org/10.1016/j.solener.2020.11.056.

[32] T. Gholaminejad, A. Khaki-Sedigh, Stable data-driven koopman predictive control: Concentrated solar collector field case study, IET Control Theory Appl. (2023) http://dx.doi.org/10.1049/cth2.12442.

[33] A.J. Gallego, M. Macías, F. de Castilla, A.J. Sánchez, E.F. Camacho, Model predictive control of the mojave solar trough plants, Control Eng. Pract. 123 (2022) 105140, http://dx.doi.org/10.1016/j.conengprac.2022.105140.

[34] D.Y. Goswami, F. Kreith, J.F. Kreider, Principles of Solar Engineering, CRC Press, 2000.

[35] T.J. Teleszewski, M. Żukowski, D.A. Krawczyk, A. Rodero, Analysis of the applicability of the parabolic trough solar thermal power plants in the locations with a temperate climate, Energies 14 (2021) http://dx.doi.org/10.3390/en14113003.

[36] A. Sánchez-Amores, J. Martinez-Piazuelo, J.M. Maestre, C. Ocampo-Martinez, E.F. Camacho, N. Quijano, Coalitional model predictive control of parabolic-trough solar collector fields with population-dynamics assistance, Appl. Energy 334 (2023) 120740, http://dx.doi.org/10.1016/j.apenergy.2023.120740.

[37] P. Velarde, A.J. Gallego, C. Bordons, E.F. Camacho, Scenario-based model predictive control for energy scheduling in a parabolic trough concentrating solar plant with thermal storage, Renew. Energy (2023) http://dx.doi.org/10.1016/j.renene.2023.02.114.